



Broadband and broadangle SPP antennas based on plasmonic crystals with linear chirp

SUBJECT AREAS:
OPTICAL MATERIALS
SPECTROSCOPY
IMAGING
OPTICAL PHYSICS

J.-S. Bouillard¹, S. Vilain*, W. Dickson¹, G. A. Wurtz¹ & A. V. Zayats¹

¹Nano-optics and Near-field Spectroscopy Laboratory, Department of Physics, King's College London, Strand, London WC2R 2LS, United Kingdom.

Received
24 September 2012

Accepted
8 October 2012

Published
20 November 2012

Correspondence and requests for materials should be addressed to J.S.B. (jean-sebastien.bouillard@kcl.ac.uk)

* Current address: 22-307 Seoul National University 599 Gwanak-ro Gwanak-gu Seoul KOREA 151-747

Plasmonic technology relies on the coupling of light to surface electromagnetic modes on smooth or structured metal surfaces. While some applications utilise the resonant nature of surface polaritons, others require broadband characteristics. We demonstrate unidirectional and broadband plasmonic antennas with large acceptance angles based on chirped plasmonic gratings. Near-field optical measurements have been used to visualise the excitation of surface plasmon polaritons by such aperiodic structures. These weakly aperiodic plasmonic crystals allow the formation of a trapped rainbow-type effect in a two-dimensional geometry as surface polaritons of different frequencies are coherently excited in different locations over the plasmonic structure. Both the crystal's finite size and the finite lifetime of plasmonic states are crucial for the generation of broadband surface plasmon polaritons. This approach presents new opportunities for building unidirectional, broadband and broad-angle plasmonic couplers for sensing purposes, information processing, photovoltaic applications and shaping and manipulating ultrashort optical pulses.

The widespread use of plasmonic devices relies significantly on our ability to control the dispersion of surface plasmon polariton (SPP) waves on nanostructured surfaces. Being surface electromagnetic waves originating from the resonant excitation of the free electron density in metals, SPPs show strong field confinement and enhancement. These characteristics suggest a broad range of applications encompassing bio- and chemical sensing, signal guiding and manipulation on subwavelength scales, and extend to include photonic devices with enhanced performance, such as photodetectors, solar cells and light emitting diodes¹⁻⁵. Recently, applications for plasmonic systems have emerged in the technologically significant area of high density data storage, where plasmon modes can, for example, provide nanofocusing of intense laser light for local heating of the recording media. In parallel, nanostructures with designer optical dispersion are required for the implementation of novel optical metamaterials for optical cloaking applications and signal processing⁶⁻⁸.

While some applications utilise the resonant nature of surface plasmon polaritons, others demand broadband characteristics. Plasmonic devices can in general support SPPs in a broad spectral range below the surface plasmon frequency, it is however difficult to achieve efficient excitation of SPPs simultaneously at different wavelengths. Practically, the excitation under omnidirectional incidence will be of great importance allowing focused beam excitation and robustness against beam alignment. Resonant structures, such as plasmonic crystals which are based on periodic arrays of holes, slits or indentations, provide very efficient coupling of light to SPP modes as well as control over the crystal's dispersion via Bloch mode formation on the periodic metal surface⁹⁻¹³. However, the inherent limitation of the crystal originates from the periodicity itself, satisfying resonant coupling conditions between free-space radiation and SPP Bloch modes over a relatively narrow spectral bandwidth. On the other hand, non-resonant structures, e.g., single slits, provide broadband free-space radiation to SPP Bloch mode coupling, albeit with relatively low efficiency^{5,14,15}.

In this paper, we study the optical properties of a weakly aperiodic plasmonic crystal, consisting of a system of slits with a linearly varying separation. This structure has been shown to achieve broadband and unidirectional excitation of SPPs, even at normal incidence, with spectral control over SPP modes formation and propagation. This leads to a plasmonic rainbow effect where the excitation of SPP modes at different frequencies occurs in spatially different locations on the structure. These modes provide a broadband source for the excitation of SPP waves on the smooth metal film surrounding the structure. The spectral position and the bandwidth of the excited waves are determined by the chirp, size of the structure and lifetime of the SPP modes of the crystal. Plasmonic band-gap formation in finite size periodic and aperiodic crystals is also discussed. The broadband plasmonic



functionality of the device is important for many applications including photovoltaics, sensing and optical information processing where wavelength multiplexing provides significant advantages.

Results

The linearly chirped plasmonic crystals studied in this paper consist of a one-dimensional grating of slits perforating a metal film. The separation between neighbouring slits linearly increases from $D_{12}=p$ to $D_{nm}=p+(m-1)\Delta p$, where p is the period, Δp is the chirp ($\Delta p/p \ll 1$), and m and n are integers ($n=m+1$). Figure 1 (a–c) presents schematics of the chirped plasmonic crystal and SEM images of plasmonic crystals with a periodic lattice and linear chirp. To understand the role of the chirp on the SPP band structure of the crystal, far-field and near-field optical measurements were performed and compared for both periodic and aperiodic structures.

The far-field transmission dispersions of the periodic structures (Fig. 1 d) exhibit the typical system of forbidden and allowed SPP bands corresponding to the excitation of the SPP Bloch modes on the

metal film interfaces. These have been identified using standard Bragg-scattering considerations of SPPs supported by the smooth film¹⁶ (as described in Methods) and the maps of the experimental and modelled field distributions related to the SPP modes (Fig. 2). For the chirped structures, despite the spatially varying slit separation, the far-field transmission still shows evidence of Bragg scattered SPP modes over a broader range of frequencies than for the periodic structures where the band extrema are related to the minimum and maximum periods present in the chirped crystal (Fig. 1 e–g). Due to the asymmetry of the chirped crystal, the SPP band structure is asymmetric with respect to the SPP propagation in up-chirp and down-chirp directions (Fig. 1 j). Compared to the periodic crystal, the bands are less defined with a broadened band-gap and a decreased density of states within the allowed SPP bands. This is a consequence of smeared phase-matching conditions for surface waves introduced in the crystal by the varying period. Numerical simulations of the local dispersion of the crystals confirm that the main origin of the broadening is inhomogeneous and primarily

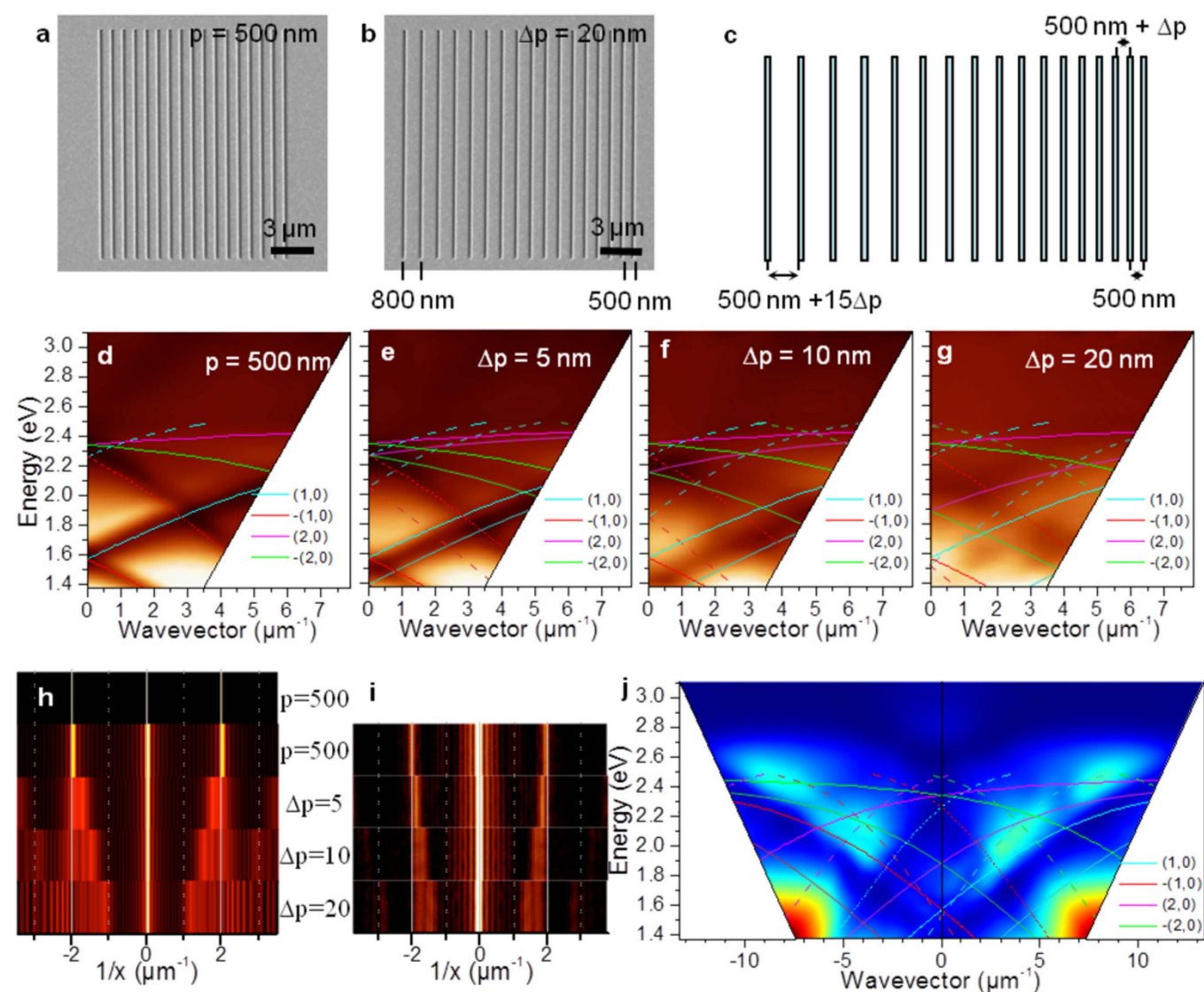


Figure 1 | Chirped plasmonic crystals and their SPP mode structure. (a,b) SEM images of the plasmonic crystal with a period of 500 nm and the chirped plasmonic crystal with $p = 500$ nm and $\Delta p = 20$ nm, respectively. (c) Schematics of the chirped structure. (d–g) Experimental far-field dispersion plots for the plasmonic crystal with period 500 nm and the chirped crystals with $p = 500$ nm and $\Delta p = 5$ nm, $\Delta p = 10$ nm and $\Delta p = 20$ nm, respectively. The calculated Bragg scattered SPP modes at the Au-air interface corresponding to the 2 extreme slit separations in each structure have been superposed onto the experimental dispersions. (h,i) Spatial frequency spectra calculated with Fourier transform of the infinite crystal (h) and the experimental structures (i). (j) Calculated dispersion (for incident angles from -45 degrees to $+45$ degrees in glass) for the structure with $\Delta p = 10$ nm.

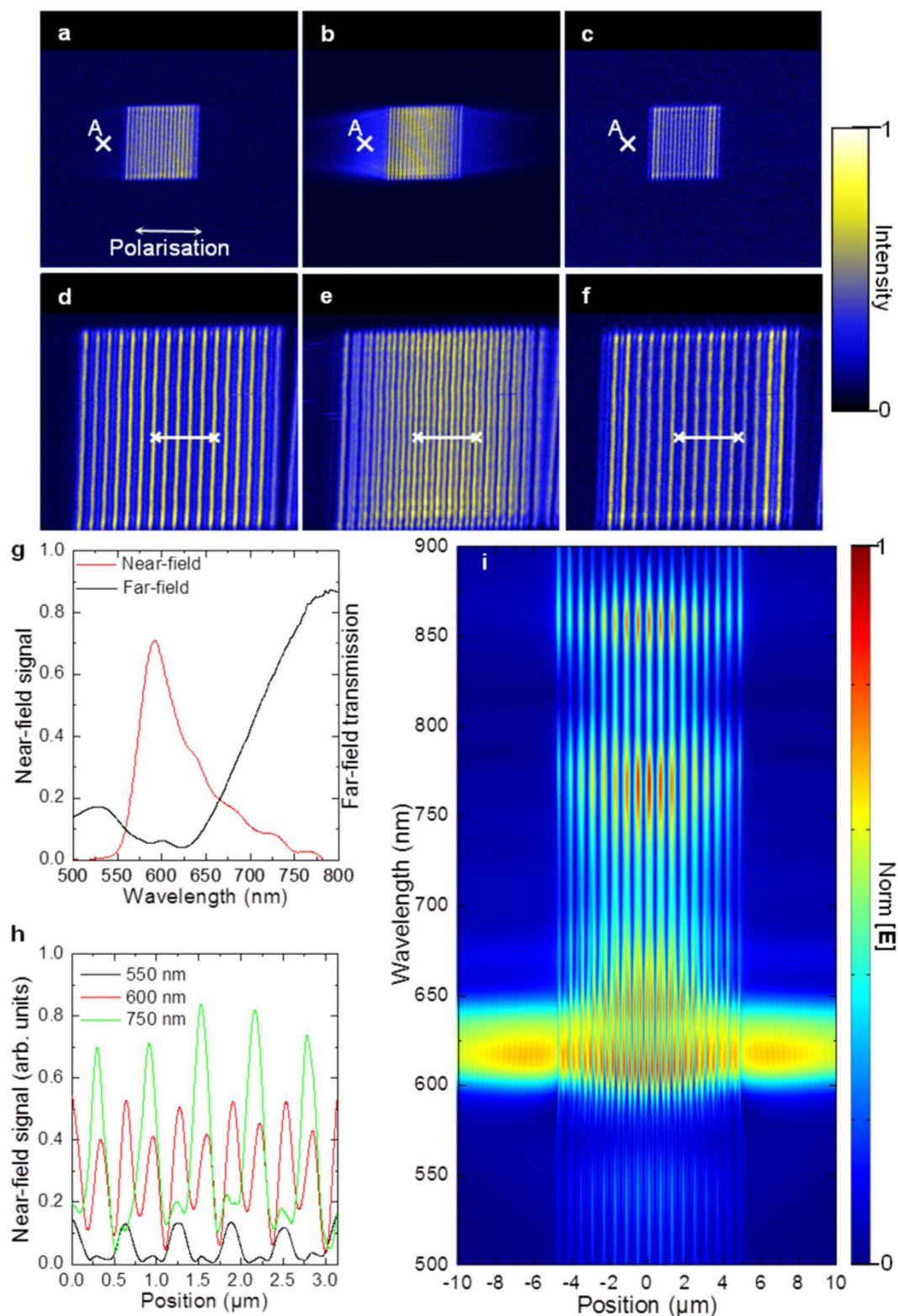


Figure 2 | Near-field optical properties of finite-size plasmonic crystals. (a–f) Near-field intensity distributions for the 1D plasmonic crystal with a period of 600 nm and a slit width of 100 nm. For all the images, the polarization is horizontal as indicated on (a). (a–c) SNOM images extracted from the movie M1. The scan size is 40 μm by 40 μm . (d–f) SNOM images extracted from the movie M2. The scan size is 13 μm by 13 μm . (g) Far-field and near-field transmission spectra of the crystal. The near-field spectrum corresponds to point A indicated in the images (a–c). (h) cross-sections of the near-field intensity distributions measured along the white line in (d–f). (i) 2D representation of cross-sections of the numerically simulated field $|E|$ plotted 20 nm above the gold film for different wavelengths. The crystal is located between $-5 \mu\text{m}$ and $5 \mu\text{m}$.

determined by the position-dependent band structure which is averaged in the far-field transmission measurements. The spatial dependence of the band structure is a direct consequence of the finite

lifetime of SPP modes in the crystal. The lifetime determines the SPP propagation distance, L_{SPP} , along the structure interfaces, generally limited to a fraction of the crystal's length, so that the conditions for



Bragg scattering (corresponding to the average local period) are only satisfied locally for several slits. This results in a plasmonic band structure that is position-dependent within the chirped crystal. For the structure with the strongest chirp ($\Delta p/p=0.04$), SPP bands are no longer clearly distinguishable in the far-field dispersion.

The false movies M1, M3 and M5 (M2 and M4 present smaller scans for M1 and M3, respectively) show the wavelength dependence of the near-field intensity distribution for the periodic grating ($p=600$ nm) and the antennas with chirp $\Delta p=10$ nm and $\Delta p=20$ nm, respectively, measured using hyperspectral scanning near-field optical microscopy. A set of representative snapshots from the movies for both the periodic and chirped crystals are shown in Figs. 2 (a–f) and 3 (a–f), respectively. One can clearly identify the narrowband excitation of SPPs on the smooth surface with the periodic structure having a full-width at half maximum (FWHM) of 40 nm. The chirped structures provide a significantly broader spectral range of smooth film SPP excitation with a FWHM of 70 nm and 190 nm for the $\Delta p=10$ nm and $\Delta p=20$ nm gratings, respectively. Compared to the periodic grating with $p=600$ nm, the SPP excitation efficiency increases by 6% and 60% for the chirped structures with $\Delta p=10$ nm and $\Delta p=20$ nm, respectively, when integrated over the entire spectral range. The chirped gratings offer almost one order of magnitude average increase in the coupling efficiency across a wide spectral range, from 650 nm to 900 nm, while at the specific wavelength corresponding to the maximum coupling efficiency of the periodic grating, $\lambda=625$ nm, the drop in coupling efficiency is about 30% for $\Delta p=10$ nm and 65% for $\Delta p=20$ nm.

Discussion

Near the crystal boundaries, the conditions for the Bloch mode excitation are broken as the crystal meets the adjacent smooth film. Scattering at the boundaries leads to the SPP Bloch modes transmission from the crystal onto the smooth film at the frequencies matching the smooth film SPPs with no restriction on momentum since the Bloch modes are normally incident on the boundary. The SPP mode coupling is a consequence of the finite size of plasmonic structures, which has a significant influence on the SPP crystal's optical properties. In particular, it impacts the far-field transmission, the energy stored within the crystal, and the SPP band-gap formation in both periodic and chirped crystals. In the case of the periodic crystal, at normal incidence, the conditions for SPP launching on the smooth film correspond exactly to the spectral range of the band-gap in the centre of the Brillouin zone (Eq. 1). This is observed in the near-field spectrum measured at point A on the smooth surface (Fig. 2 g), where the spectral components absent from the far-field transmission spectrum are present in the near-field being coupled to the SPP modes on the smooth film. As seen from the experiment (M1, Fig. 2 a–f) and confirmed by the simulations of the near-field distribution for the crystal (Fig. 2 i), at the wavelengths shorter than the lattice period relatively small near-field intensity and far-field transmission are observed (cf. Fig. 1d, 2d, 2i). As the wavelength increases, a clear Bloch mode structure appears in the centre of the crystal (Fig. 2 e, h, i) having a characteristic intensity distribution with a period twice that of the crystal lattice as expected for a $(\pm 1,0)$ mode¹⁷.

The near-field images and the modelled field maps provide evidence of plasmonic band gap formation near the crystal's boundaries despite the broken symmetry of the lattice (Fig. 2). It is also clear from the spectral position of the higher band-edge, which experiences a red-shift, that the mode splitting is weaker at the crystal's boundaries leading to a narrower bandgap (Fig. 2 i, M6). Near the crystal boundary, if the crystal size is larger than the SPP propagation length, determined by their lifetime, the SPP modes sample only part of the spectral composition of the weakly periodic lattice (Fig. 1 h,i), and, thus, experience a position-dependent change in their effective refractive index $n_{SPP}(\omega, x) = c k_{SPP}(\omega, x)/\omega$, where x is the position

on the structure, c is the speed of light in vacuum and ω is the frequency of incident light. Therefore, for plasmonic crystals of finite size, near the boundaries of the crystal, SPP Bloch modes are efficiently formed despite the imbalance in intensity and wavevector from counter-propagating plasmonic modes¹⁰. SPP modes propagating in the direction towards the crystal boundary will experience a gradual increase in their refractive index $dk_{SPP}(\omega, x)/dx > 0$. This is clearly observed in Fig. 2 (i) with the mode corresponding to the lower SPP Bloch mode in the centre of the crystal (Fig. 1 d) coupling to the smooth film SPP at the frequency for which their effective refractive indices match (see movie M6). The number of slits contributing to the smooth film SPP generation is determined by the lifetime of the SPP modes and in the visible spectral range corresponds to about 7–8 slits (Fig. 2 e, i).

Similarly, in the case of the chirped plasmonic crystals, the SPP modes originate from Bragg scattering by a number N of slits depending on the SPP lifetime at the resonant wavelength determined by the effective average period \bar{D} . The spatial frequency spectrum of the chirped structure is similar to the frequency spectrum of a periodic structure of finite size (Fig. 1 h,i). However, the control over this spectrum provided by the chirp allows the dispersion of the SPP mode to be engineered in the vicinity of the structure boundary in order to optimize the efficiency and bandwidth of coupling to the smooth film SPP. In contrast to periodic crystals, however, the excitation of SPP modes at different wavelengths is now observed at different locations within the structure (Fig. 3). This is accompanied by the characteristic SPP Bloch-mode profile observed in the near-field of the structure (Fig. 3 g, h, cf. Fig. 2 h,j). For the chirped grating considered here, the SPP lifetime is essentially unchanged from the periodic crystal and was estimated from the experimental data to correspond to a propagation length of about $1/2\text{Im}(k_{SPP}) \approx 5$ μm at a free-space wavelength of 625 nm. As a result, the spatial extent of the resonant excitation of SPP Bloch modes is on the order of 5 μm , which corresponds to approximately eight slits contributing to the phase-matching process at this wavelength ($N=8$). For $\Delta p=10$ nm and $\Delta p=20$ nm, this distance will include variations in slit separation of 80 nm and 160 nm, respectively, which introduces the broadband behaviour observed in the coupling to the smooth film SPPs. The spatial localisation of the excitation can be directly observed in the experimental near-field maps (Fig. 3 a–f). The wavelength-sensitive spatial position of the resonance follows qualitatively that of Eq. (1) as a function of period and angle of incidence.

Thus, for each wavelength within the working range of the chirped crystal (determined by maximum and minimum separation between the slits), the resonance occurs at the location within the structure where the average period satisfies the resonant conditions of Eq. (1). The effect is similar to the trapped rainbow effect observed in slow-light photonic systems^{18,19}. As discussed above, the SPP lifetime will determine the number of contributing slits and, thus, the efficiency of SPP mode formation. If, however, the lifetime is large enough for the SPP to sample the entire crystal ($L \approx L_{SPP}$), the central wavelength will be determined by the average crystal period with the maximum intensity in the centre of the crystal. The chirp in this case determines the width of the excited SPP spectrum. In this situation, the excited SPPs will be outcoupled to smooth film SPPs at the boundary of the crystal in a broad spectral range around the resonant wavelength for $\bar{D} = p + (M-2)\Delta p/2$ with the bandwidth $(M-2)\Delta p$, where M is the number of slits forming the crystal. The relative amplitude of the coupled components will be weighted by the propagation loss before reaching the crystal boundary. If the losses prevent the utilisation of the whole bandwidth of the antenna by limiting the number of contributing slits, $N < M$, the bandwidth will be reduced to approximately $(N-2)\Delta p$ with the spectrum centred around the wavelength corresponding to the average period $\bar{D} \approx p \pm \Delta p/(2p)L_{SPP}$, where the positive or negative sign correspond to a down- or up- chirp, respectively. This equation provides the

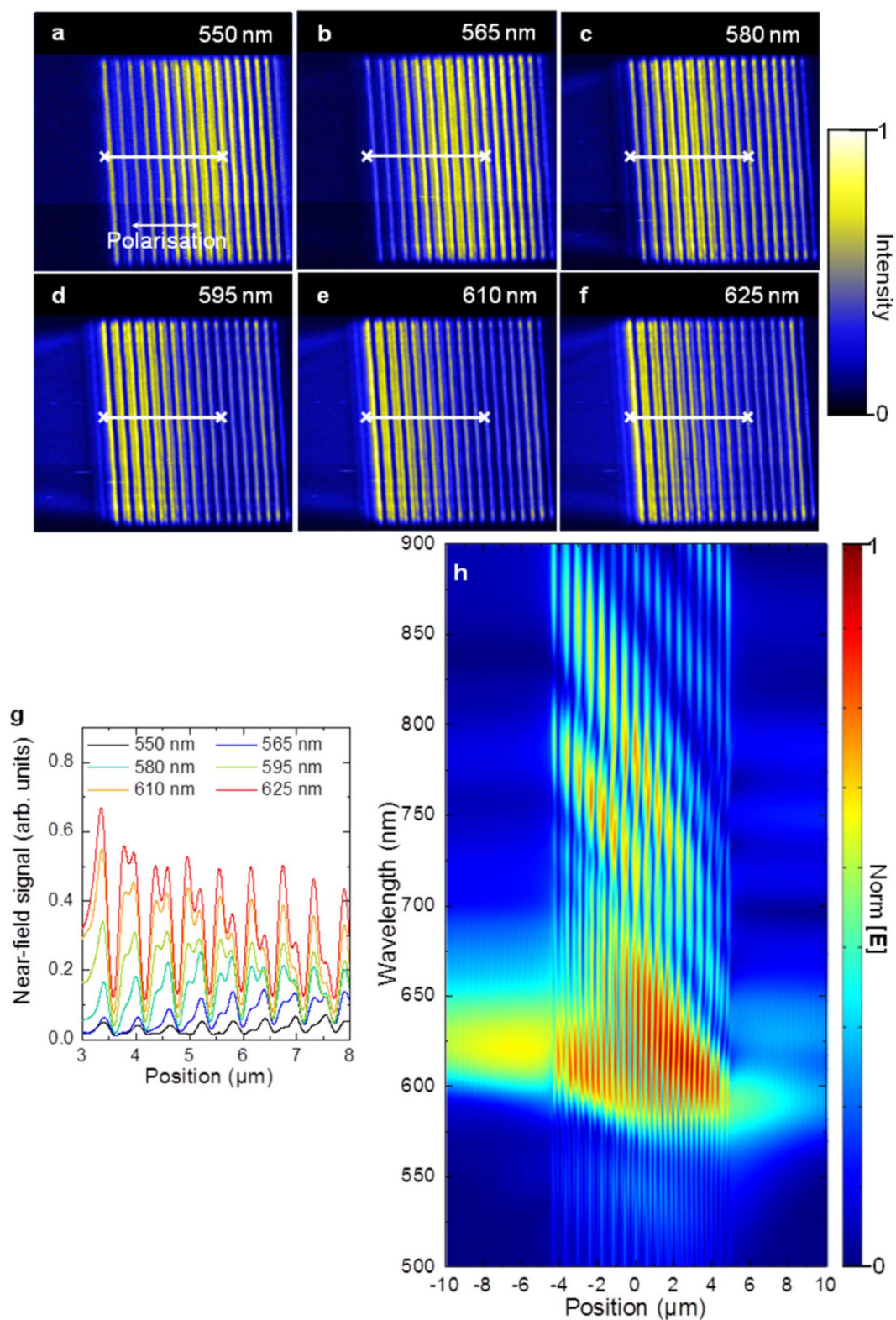


Figure 3 | Near-field optical properties of chirped plasmonic crystals. (a–f) Near-field intensity distributions for the chirped crystal with $p = 500$ nm and $\Delta p = 10$ nm and the slit width of 100 nm. The two extreme slit separations for this structure are 500 nm and 650 nm. For all the images, the polarisation is horizontal as indicated in (a). The images are extracted from the movie M4. The scan size is 13 μm by 13 μm . (g) The intensity cross-sections measured from the images (a–f) as indicated by the white line. (h) 2D representation of cross-sections of the numerically simulated field $|E|$ plotted 20 nm above the gold film for different wavelengths. The crystal is located between -5 μm and 5 μm .

self-consistent relation between the resonant SPP wavelength and SPP lifetime for $L < L_{SPP}$.

The same principle that was applied to the wavelength independent excitation above can be applied to the engineering of angle

independent coupling. If the spectral bandwidth of the antenna can be estimated from the SPP bandgap broadening at a given angle of incidence (the analysis above was done on the example of the normal incidence), the range of working angles can be estimated from the



wavevector range corresponding to the bandgap edges at a given wavelength. Physically, the effect is the same as for broadband unidirectional excitation; monochromatic light having different incident angles with respect to the chirped crystal will be coupled to SPP Bloch modes at different spatial locations on the crystal. As before, Bloch modes can then propagate towards the crystal boundary, thus achieving coupling of light to smooth film SPPs over a broad range of incident angles. As one can see from the experimental dispersions (Fig. 1 d–f) and numerical modelling, (Fig. 4 d–f) the chirped crystals provide a range of incidence angles about 3 times broader for SPP excitation than periodic crystals. Moreover, the

asymmetry of their dispersion with respect to down-chirp and up-chirp propagation provides directionality of the coupling at oblique angles. This effect may explain the higher coupling efficiency observed experimentally in Fig. 4 (b) for chirped gratings, as in the experiment the incident beam is slightly focused. It is interesting to note a colourless excitation of the SPPs by the $\Delta p = 20$ nm structure at the angle of about 40° covering the wavelength range from 600 nm to almost 1000 nm (Fig. 4f).

The chirped grating designed with the minimum separation, corresponding to resonant conditions around 500 nm, will act as a unidirectional broadband launcher of SPPs for wavelengths longer

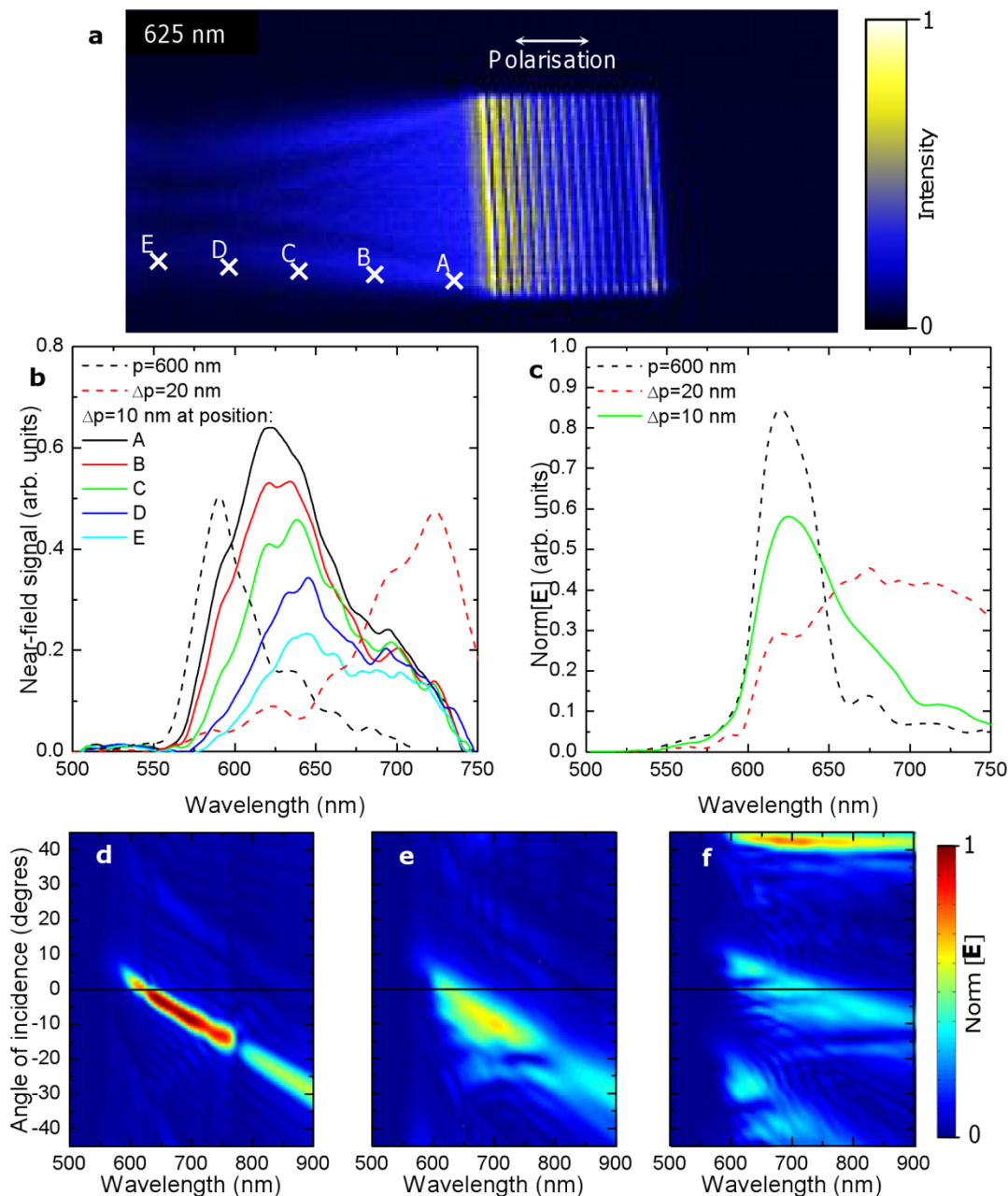


Figure 4 | SPP coupling efficiency. (a) Near-field intensity distribution at the wavelength of 625 nm for the chirped plasmonic crystal with $p = 500$ nm and $\Delta p = 10$ nm and the groove width of 100 nm. The polarisation is horizontal as indicated on (a), and the shortest period is on the right hand side of the nanostructured area. The image was extracted from the movie M3. The scan size is 40 μ m by 18 μ m. (b) Near-field spectra extracted at various points on the smooth gold film from M3 and corresponding near-field spectrum (at point A) for the crystal with 600 nm period and the chirped crystal with $p = 500$ nm and $\Delta p = 20$ nm. (c) Numerically simulated near-field spectra (20 nm from the Au surface) at the distance 5 μ m from the crystal boundary for the crystal with 600 nm period and the chirped crystals with $p = 500$ nm and $\Delta p = 10$ nm and $\Delta p = 20$ nm. (d–f) Simulated spectra for different incidence angles of the SPP intensity on the gold-air interface measured 5 μ m from the boundary of the structure for the periodic $p = 600$ nm (d) and chirped $\Delta p = 10$ nm (e) and $\Delta p = 20$ nm (f) crystals.



than 500 nm. Since gold does not support SPPs around this wavelength due to the interband transition resonance and associated strong losses, no SPPs will be excited at this boundary of the structure on the Au-air interface. In practice, the achievable bandwidth will be determined by the interplay of the SPP propagation length at the given wavelength and the length of the structure required to achieve the necessary down-chirp. The SPPs excited at shorter wavelengths will reach the outcoupling facet of the antenna already partly attenuated and will contribute to the smooth film SPP less efficiently. In accordance to the consideration above, the increase of the chirp leads to an increase of excitation bandwidth (Fig. 4) and also to the red shift of the dominating wavelength, thus favouring the excitation of long-wavelength SPPs, as observed for the antenna with the larger chirp. This is confirmed in the near-field spectra measured on the smooth metal surface, where broadband unidirectional excitation of the SPP has been achieved with the chirped gratings with a bandwidth more than 2 times larger than for the periodic crystal and with a similar efficiency (Fig. 4). During the propagation on the smooth surface, there is a redistribution of the spectral components as the distance from the grating increases, due to the different propagation lengths of SPPs at different frequencies (Fig. 4).

In conclusion, we have described a unidirectional, broadband and broad acceptance angle antenna for coupling incident light to surface plasmon polaritons based on a plasmonic crystal with linear chirp. In order to understand the behaviour and design rules of such antennas, the influence of the finite-size and the weak disorder of the crystal lattice on the formation of the SPP Bloch modes and the optical properties of the structures have been investigated. Weak variations in the periodicity lead to small changes in the Bloch mode structure over the length scales determined by the SPP propagation length, meaning that the system of allowed and forbidden SPP bands can still be formed. These modes provide efficient coupling to SPPs on the smooth metal surface over a broad range of both wavelengths and angles of incidence. Similar principles can be used to design directional wavelength demultiplexing antennas based on chirped plasmonic crystals. The chirp does not have to be linear and can be engineered to achieve fine control over the local dispersion and antenna's properties. The chirped plasmonic crystals can also be used for shaping ultrashort SPP pulses via control of the group velocity dispersion of the structure. Extension of the approach to two-dimensional chirped crystals may also reveal opportunities to precisely shape the light and SPP wavefronts similarly to arrayed plasmonic antennas of varying parameters^{7,8}.

Methods

The samples. A series of one-dimensional SPP crystals were milled using a focused ion beam (FIB) system, on a 300 nm thick gold film magnetron sputtered on a SiO₂ substrate with an 8 nm film of Ta₂O₅ used as an adhesion layer. All gratings are composed of 17 slits of 100 nm width and 10 μm length. Three gratings were milled with the separation between the slits increasing linearly from 500 nm to 575 nm, $\Delta p/p=0.01$ (sample A), 650 nm, $\Delta p/p=0.02$ (sample B) and 800 nm, $\Delta p/p=0.04$ (sample C), respectively, corresponding to chirps of 5 nm, 10 nm and 20 nm, respectively, as illustrated in Figure 1. For comparison, three other gratings were also made with fixed periods: 500 nm (sample D), 600 nm (sample E) and 700 nm (sample F).

Far-field optical spectroscopy. The light from a stabilised tungsten-halogen bulb passes through a polarising cube before illuminating the sample, through the substrate face. A pin hole is used to reduce the size of the illumination beam on the sample. A long working distance objective is used to collect the light transmitted through the structure. Some light passes through a beam splitter onto a CCD camera to visualise the area of collection on the sample surface, and the rest of the light is reflected onto an analysing polariser cube with its axis parallel to the illumination polarisation, before being coupled into a 100 μm core optical fibre. The fibre is used to guide the transmitted light to the spectrometer. Far field transmission spectra were taken at different angles of incidence every 2 degrees starting from normal incidence to 30 degrees in order to plot the transmission dispersion for each structure.

Near-field optical spectroscopy. The SPP intensity distribution was studied inside and around each structure using the hyperspectral SNOM arrangement described previously²⁰. This set up allows mapping of the near-field intensity distribution at all wavelengths in a single scan. The near-field images of the SPP intensity on each

structure were measured between 500 nm to 800 nm wavelength with 1 nm spectral resolution. The resulting data set is then analysed to present either a false movie showing the evolution of the near-field as the wavelength is varied or to recover the near-field optical transmission spectra at every position of the SNOM probe, which contains contributions of both evanescent and propagating components, in contrast to the far-field spectra that contain information only on propagating components of the transmitted field. Please note that direct comparison of the numerically calculated and experimental near-field images is not always possible as the polarisation sensitive near-field coupling to the probe is not considered in the simulations.

Modelling. Full vectorial numerical modelling of the optical properties of the structures was performed using a finite element method (COMSOL Multiphysics). The mode identification for the periodic structures was done using the empty lattice model and taking into account Bragg scattering of the smooth film SPPs by the periodic lattice¹⁶:

$$\vec{k}_{SPP-B} = \vec{k}_{SPP} + \vec{k}_B = \frac{2\pi}{\lambda_0} \sqrt{\frac{\epsilon_{Au}(\omega)\epsilon_d}{\epsilon_{Au}(\omega) + \epsilon_d}} \vec{u} + l \frac{2\pi}{d} \vec{i} + m \frac{2\pi}{d} \vec{j}, \quad (1)$$

where \vec{k}_{SPP} and \vec{k}_{SPP-B} are the SPP wave vectors before and after Bragg scattering in the periodic lattice, respectively, \vec{k}_B is the momentum contributed during the scattering by the crystal, λ_0 is the vacuum wavelength, $\epsilon_{Au}(\omega)$ and ϵ_d are the permittivities of Au and the adjacent dielectric, respectively, d is the period of the crystal with the square lattice, (l, m) are integers accounting for Bragg reflected SPPs, \vec{u} is the unit vector describing the SPP propagation direction before Bragg scattering, and \vec{i} and \vec{j} are the unit reciprocal lattice vectors of the periodic structure.

- Gramotnev, D. K. & Bozhevolnyi, S. I. Plasmonics beyond the diffraction limit. *Nature Photonics* **4**, 83–91 (2010).
- Novotny, L. & van Hulst, N. Antennas for light. *Nature Photonics* **5**, 83–90 (2011).
- Brongersma, M. L. Engineering optical nanoantennas. *Nature Photonics* **2**, 270–272 (2008).
- Atwater, H. A. & Polman, A. Plasmonics for improved photovoltaic devices. *Nature Materials* **9**, 205–213 (2010).
- Zayats, A. V., Smolyaninov, I. I. & Maradudin, A. A. Nano-optics of surface plasmon polaritons. *Physics Reports* **408**, 131–314 (2005).
- Cai, W., Chettiar, U. K., Kildishev, A. V. & Shalaev, V. M. Optical cloaking with metamaterials. *Nature Photonics* **1**, 224–227 (2007).
- Yu, N. *et al.* Light propagation with phase discontinuities: generalized laws of reflection and refraction. *Science* **334**, 333–337 (2011).
- Ni, X., Emani, N. K., Kildishev, A. V., Boltasseva, A. & Shalaev, V. M. Broadband light bending with plasmonic nanoantennas. *Science* **335**, 427 (2012).
- Laux, E., Genet, C., Skauli, T. & Ebbesen, T. W. Plasmonic photon sorters for spectral and polarimetric imaging. *Nature Photonics* **2**, 161–164 (2008).
- Bravo-Abad, J. *et al.* How light emerges from an illuminated array of subwavelength holes. *Nature Physics* **2**, 120–123 (2006).
- Mikhailov, V., Wurtz, G., Elliott, J., Bayvel, P. & Zayats, A. V. Dispersing light with surface plasmon polaritonic crystals. *Physical Review Letters* **99**, 083901 (2007).
- Benetou, M. I., Thomsen, B. C., Bayvel, P., Dickson, W. & Zayats, A. V. Four-level polarization discriminator based on a surface plasmon polaritonic crystal. *Applied Physics Letters* **98**, 111109 (2011).
- Baron, A. *et al.* Compact antenna for efficient and unidirectional launching and decoupling of surface plasmons. *Nano Letters* **11**, 4207–4212 (2011).
- Radko, I. P. *et al.* Efficient unidirectional ridge excitation of surface plasmons. *Optics Express* **17**, 7228–7232 (2009).
- Laluet, J.-Y. *et al.* Optimization of surface plasmons launching from subwavelength hole arrays: modelling and experiments. *Optics Express* **15**, 3488–3495 (2007).
- Dickson, W., Wurtz, G. A., Evans, P. R., Pollard, R. J. & Zayats, A. V. Electronically controlled surface plasmon dispersion and optical transmission through metallic hole arrays using liquid crystal. *Nano Letters* **8**, 281–286 (2008).
- Darmanyan, S. A., Nevière, M. & Zayats, A. V. Analytical theory of optical transmission through periodically structured metal films via tunnel-coupled surface polariton modes. *Phys. Rev. B* **70**, 75103 (2004).
- Tsakmakidis, K. L., Boardman, A. D. & Hess, O. “Trapped rainbow” storage of light in metamaterials. *Nature* **450**, 397–401 (2007).
- Gan, Q., Ding, Y. & Bartoli, F. “Rainbow” trapping and releasing at telecommunication wavelengths. *Physical Review Letters* **102**, 056801 (2009).
- Bouillard, J.-S., Vilain, S., Dickson, W. & Zayats, A. V. Hyperspectral imaging with scanning near-field optical microscopy: applications in plasmonics. *Optics Express* **18**, 16513–16519 (2010).

Acknowledgements

This work has been supported by FP7 STREP PLAISIR and EPSRC (UK). The authors are grateful to P. Ginzburg and D. O'Connor for stimulating discussions.

Author contributions

All authors contributed equally to this work, prepared and reviewed the manuscript.



Additional information

Supplementary information accompanies this paper at <http://www.nature.com/scientificreports>

Competing financial interests: The authors declare no competing financial interests.

License: This work is licensed under a Creative Commons Attribution-NonCommercial-NoDerivs 3.0 Unported License. To view a copy of this license, visit <http://creativecommons.org/licenses/by-nc-nd/3.0/>

How to cite this article: Bouillard, J.-S., Vilain, S., Dickson, W., Wurtz, G.A. & Zayats, A.V. Broadband and broadangle SPP antennas based on plasmonic crystals with linear chirp. *Sci. Rep.* **2**, 829; DOI:10.1038/srep00829 (2012).